

# Normal and superconducting phase diagram of Oxygen-implanted Aluminum thin films: similarity with granular films and influence of kinetics of defects

E. H. C. P. Sinnecker, M. M. Sant'Anna, and M. ElMassalami

*Instituto de Física, Universidade Federal do Rio de Janeiro,  
Caixa Postal 68528, 21941-972 Rio de Janeiro RJ, Brazil*

Traditionally, superconductivity of ion-irradiated thin films has been investigated along lines that are distinctly different from those of granular thin films although both exhibit similar effects. Also, none of these effects has been correlated with the kinetics of defects (interstitials, vacancies, etc.) even when these are introduced by a violent damage-causing process such as a chemically-active-ion irradiation. We show, based on analysis of electrical properties of oxygen-implanted Aluminum thin film, that the normal-state and superconducting  $T-x$  phase diagram of irradiated films is the same as that of granular ones ( $x$  is a measure of the influence of defects). These phase diagrams are dominated by three boundaries: an enhancement of superconductivity with a transition at  $T_c(x)$ , a Kondo behavior with a minimum at  $T_K^{\min}(x)$ , and a negative curvature resistivity with a maximum at  $T_{\text{NCR}}(x)$ . Moreover, we identify an additional thermally-activated relaxation process which is traced down to the kinetics of stabilized charges and defects. Analysis of thermal and temporal evolution of such kinetics, as manifested in the magnetoresistivity, allows us to relate the enhancement of  $T_c(x)$  to an induced lattice softening,  $T_K^{\min}(x)$  to an induced color-centre-type magnetic moment, and  $T_{\text{NCR}}(x)$  to kinetics of impurity-stabilized electric charges and defects.

PACS numbers: 72.15.Lh, 74.62.Dh, 72.15.Qm, 74.81.Bd

## I. INTRODUCTION

Controlled incorporation of disorder or defects in metallic system is known to imprint strong influences on their thermal, magnetic and electronic properties. Features such as lattice softening, Kondo effect and electronic localization are well known. Two other manifestations, less known and even counter-intuitive, are an order-of-magnitude enhancement of superconducting transition temperature<sup>1</sup> and a high-temperature negative-curvature resistivity.<sup>2</sup> Such a rich cascade of disorder/defect-induced features are usually captured within a  $T-x$  phase diagram ( $x$  is a tunable control parameter).

Metallic thin films<sup>3,4</sup> provide a simple model for studying such phase diagrams. Controlled defect/disorder incorporation in such films can be conveniently introduced (i) during the film growth whereat the evaporation-deposition process is undertaken in a controlled ambient of, the to-be incorporated, gas; a *granular* film is the special case wherein nano-sized metallic grains with varying sizes are separated from each other by a nonmetallic interface.<sup>2-4</sup> (ii) Atomic implantation in an already-grown thin film; in these *irradiated* films, randomly and homogeneously distributed disorder/defects can be created by a variety of projectiles.<sup>5-7</sup>

With no loss of generality, this work constructed and analyzed a  $T-x$  phase diagram of Aluminum thin films after injecting defect/disorder by successive oxygen irradiation at ambient temperature (see Appendix A). We opted for oxygen implantation since this would allow us to probe and identify processes associated with the incorporation of this *chemically-active* entity. The choice of

Aluminum, on the other hand, allows us to overcome our present experimental beam limitation by extrapolating  $x$  to other regions that had already been studied in the seminal works on granular<sup>2,3,8,9</sup> and irradiated films.<sup>5-7</sup>

Let us recall that oxygen irradiation of an Al film is a violent process that leads to an unstable, non-equilibrium, thermodynamical state. A drive towards equilibrium by energy minimization requires an activation of some relaxation channels. We follow the manifestation of such processes by measuring the resistivity,  $\rho(t, T, H, n^{th})$ , as a function of time, temperature, magnetic field, and fluence of various,  $n^{th}$ , irradiation sessions (see Appendices A-C). Based on the analysis of these  $\rho(t, T, H, n^{th})$  curves, we construct the phase diagram and identify its main boundaries, namely a negative curvature resistivity, a Kondo behavior and an enhanced superconductivity.

We identify two classes of relaxation processes: one associated with conventional disorder/defects-related relaxation processes as in pure Al [Ref.10] and a novel one associated with the kinetics of defects induced by O-implantation (as damage-causing projectile or as an oxidizing agent that eventually leads to a formation of  $\text{Al}_2\text{O}_3$ ;<sup>11</sup> these in turn leads to a stabilization of irradiation-induced defects). This latter class is singled out as the one that shapes the phase diagram. One of the major conclusions of this work is that the overall evolution of the phase diagrams of granular<sup>2-4</sup> and irradiated<sup>5-7</sup> films is similar: an indication of a similarity of the essential kinetics involved in the aftermath of oxygen incorporation.

## II. RESULTS AND DISCUSSION

### A. Negative Curvature Resistivity (NCR)

Figure 1 indicates that all  $\rho(1.7 \leq T \leq 315 \text{ K}, n^{\text{th}})$  are metallic, without any traces of the so-called recovery stages usually observed in irradiated/quenched Aluminum samples:<sup>10</sup> indeed, this O-irradiation was undertaken at ambient temperature which is well above the temperature ranges of the three recovery stages.<sup>10</sup> Nevertheless,  $\rho(T > 300 \text{ K}, n^{\text{th}})$  exhibits a sub-linear deviation that develops, at higher temperature, into a negative curvature resistivity with a peak maximum at a characteristic temperature  $T_{\text{NCR}}$ . This deviation, away from linearity, is much accelerated above  $T_{\text{NCR}}$  (which decreases as disorder is increased by subsequent  $n^{\text{th}}$  irradiation). That this thermally activated NCR process is not related to a recovery stage III of pure Al can be seen in Fig. 2(a) which shows that although  $\rho(T > T_{\text{NCR}}, 7^{\text{th}})$  is monotonically decreased as  $T \rightarrow 315 \text{ K}$  (the maximum available upper limit), on cooling directly afterwards,  $\rho(T, 7^{\text{th}})$  climbs upwards.

Another intriguing feature of this NCR process is the manifestation of a slow aging (in days) of both the position of  $T_{\text{NCR}}$  and the magnitude of  $\rho(T_{\text{NCR}})$ . Such an effect, related to the second class of relaxations, rules out any interpretation in terms of crystalline electric field splitting such as the one observed in Ce-based compounds.<sup>12</sup> Fig. 3(a) indicates that the conductivity enhancement ( $T > T_{\text{NCR}}$ ) occurs concomitantly with a surge of a decrease in the magnitude of Hall coefficients. We consider this NCR process to be driven by a disassociation of impurity-stabilized electric charges and that the aging process is associated with the kinetics of these impurities (for more details see Appendix D). We observed that after a time of the order of months,  $\rho(T, 7^{\text{th}})$  traverses the NCR peak reversibly. Such a non-hysteric NCR (though with a lower  $T_{\text{NCR}}$ ) can be identified in the reported results of granular Al films.<sup>2</sup> Both the reported and our  $T_{\text{NCR}}$  are plotted in Fig. 4; their smooth evolution across the ranges of granular and irradiated films is a testimony to the similarity of the mechanism behind the NCR.

### B. Kondo effect

On lowering the temperature much below  $T_{\text{NCR}}$ , we observed no time variation in  $\rho(t, T < T_{\text{NCR}}, 7^{\text{th}})$  even when the sample is repeatedly recycled within the range  $T < T_{\text{NCR}}$ . Nevertheless, the influence of subsequent irradiation is not just a monotonic upward shift of the whole  $\rho(T, n^{\text{th}})$  curve [identifiable as an increase in  $\rho_{300\text{K}}(n^{\text{th}})$  and  $\rho_0(T \rightarrow 0 \text{ K}, n^{\text{th}})$ ]. Rather, there are additional irradiation-induced low-temperature features, namely a *log-in-T* feature and an enhancement in both  $T_c$  and  $\left(\frac{\partial \rho}{\partial T}\right)_{100-220 \text{ K}}$ . Fig. 2(b) and insets of Fig. 4 indi-

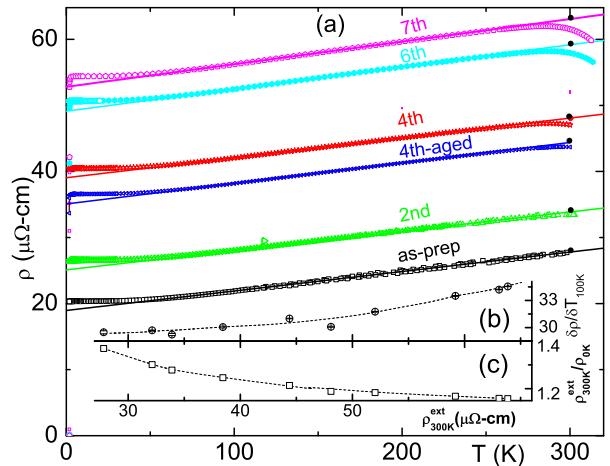


FIG. 1. (a) Representative  $\rho(T, n^{\text{th}})$  curves. For the  $4^{\text{th}}$ -irradiation, two  $\rho(t, T, 4^{\text{th}})$  curves are shown, one measured directly after irradiation while the other measured after 40 days, during which the sample had been left at ambient temperature, exposed to air: these, together with the five  $\rho(t, T, 7^{\text{th}})$  curves of Fig. 2 reveal the action of the second-class relaxation processes. The solid lines are linear fit with a slope  $(\partial\rho/\partial T)_{100-220\text{K}}$ . (b) Evolution of  $(\partial\rho/\partial T)_{100-220\text{K}}$  (in units of  $\text{n}\Omega\text{-cm}$ ) as a function of  $\rho_{300\text{K}}^{\text{ext}}$  (represented by solid black circles in main panel). (c) The RRR ratio  $\frac{\rho_{300\text{K}}^{\text{ext}}}{\rho_{0\text{K}}}$  decreases steadily with the  $n^{\text{th}}$  irradiation; these values are similar to the ones reported for granular films.<sup>2</sup>

cate that as  $T \rightarrow T_c^+$ ,  $\rho(T, 5\text{kOe} > H_{c2}, n^{\text{th}})$  is weakly increased with a *log-in-T* thermal evolution. This excess resistive contribution becomes more accentuated on subsequent  $n^{\text{th}}$  irradiation [but degraded by aging as in Fig. 2(b)].

A plot of the obtained minimum points of resistivity,  $T_{\text{K}}^{\text{min}}$ , versus  $\rho_{300\text{K}}^{\text{ext}}$  in Fig. 4 evolves smoothly and extrapolates directly into a  $T_{\text{K}}^{\text{min}} - \rho_{300\text{K}}$  curve taken from Bachar *et al.*<sup>2</sup> Based on muon spin resonance and magnetoresistivities, these authors identified their  $T_{\text{K}}^{\text{min}}$  events as originating from a Kondo behavior. Based on the similarity of our  $T_{\text{K}}^{\text{min}}$  with that of the granular films<sup>2</sup> (reproduced in the right-hand side inset of Fig. 4), we attribute our *log-in-T* rise in resistivity to a surge of a Kondo behavior. Such an identification is confirmed by a negative magnetoresistivity of Fig. 3(b) wherein low-field  $\rho(T, H)$  evolves as  $\sqrt{H/T}$ .<sup>2</sup>

We associate this Kondo effect to scattering off irradiation-induced paramagnetic, color-centre-type, defects located at the interface between Al and  $\text{Al}_2\text{O}_3$  grains. Such centres were observed in irradiated  $\text{Al}_2\text{O}_3$  by electron spin resonance studies<sup>15</sup> and were attributed to either unpaired electrons which are trapped at an anion vacancy or to a hole trapped near an oxygen ion which is adjacent to  $\text{Al}^{3+}$  vacancy. On assuming that implantation has introduced complexes<sup>1</sup> (e.g.  $\text{Al}_2\text{O}_3$ ) which are capable of stabilizing these centres, one is able to explain why: (i) Kondo behavior is not observed in pure Aluminum films or even when these are irradiated with

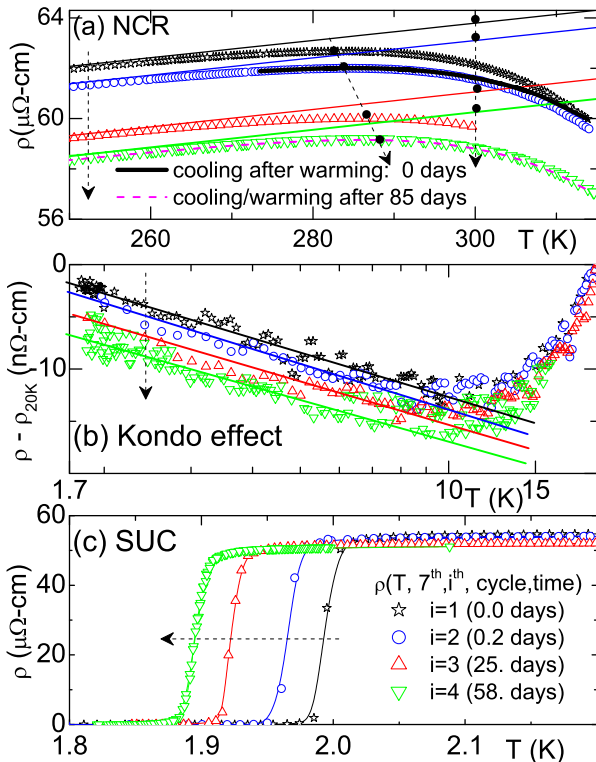


FIG. 2. Manifestation of the influence of aging on the three main features of the phase diagrams. The  $i^{th}$  cycle represents the order and time (in days) of the cooling-warming-up measurement carried out after the  $7^{th}$  irradiation session. (a) The influence of aging on the position and height of the peak maximum of NCR. The thick black line is the cooling curve directly after the first,  $i=1$ , warming-up measurement while the dashed line is the cooling and warming curves of  $i=5$  cycle after 85 days. The solid thin straight lines are linear fits within the range  $100 \leq T \leq 220$  K. The solid circles represent each of  $\rho(T_{NCR}, 0 \text{ kOe}, 7^{th}, i^{th})$  and  $\rho_{300 \text{ K}}^{ext}(0 \text{ kOe}, 7^{th}, i^{th})$ . (b) Thermal evolution of  $\rho(T, 5 \text{ kOe}, 7^{th}, i^{th}) - \rho(20 \text{ K}, 0 \text{ kOe}, 7^{th}, i^{th})$  in a semilog plot. For  $T < 20$  K, this shows a  $\log\text{-in-}T$  dependence which is not a quantum localization effect since our films do not manifest a 2-dimensional character. (c) The degradation of the superconductivity with aging. The arrows highlight the tendency of aging influence while the solid lines in panels (b) and (c) are guide to the eye. Just as for  $T_{NCR}$  of panel (a), there is no appreciable change in  $T_K^{\text{min}}$  and  $T_c$  within the interval  $58 < t < 85$  days: the curves of the  $4^{th}$  and  $5^{th}$  cycles are similar.

non-chemically-active projectiles. (ii) Kondo behavior is absent at the lower left-hand side of Fig. 4. Here the metallic and screening character are sufficiently strong to oppose the formation of paramagnetic centres. (iii) The surge, operation and manifestation of a Kondo process is similar in both the granular and irradiated films.

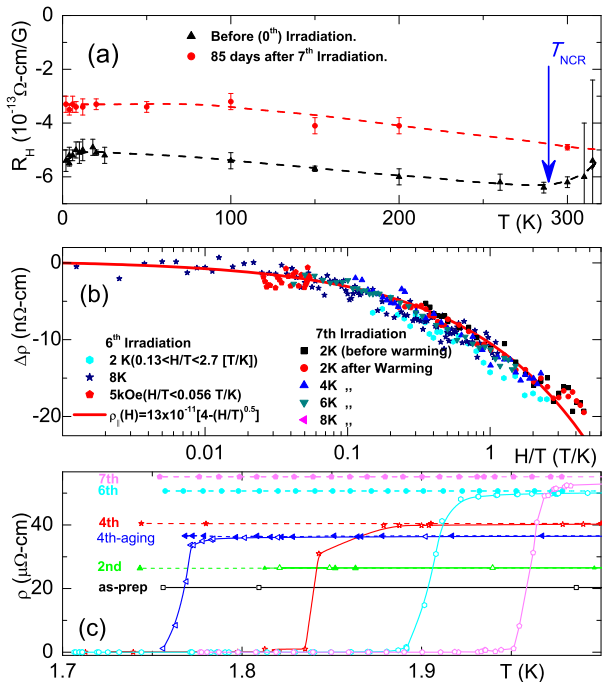


FIG. 3. (a) Hall coefficients of thin films of Al before and 85 days after the  $7^{th}$  irradiation. Notably, though the thermal evolution of both are similar, that of the irradiated sample is more negative and exhibits an upturn above  $T_{NCR}$ . (b) The negative magnetoresistivity  $\Delta\rho(H/T, n^{th}) = \rho(H/T, n^{th}) - \rho(0, T, n^{th})$  for  $n^{th} = 6, 7$  and various combination of  $H_{c2} < H < 20$  kOe and  $T_c < T < T_K^{mn}$  (small  $H/T$ ). The solid line is a fit to  $\Delta\rho(H/T, 6^{th}) \propto (H/T)^{1/2}$ . Such a  $\sqrt{H/T}$  scaling is also evident in low-resistivity granular Al thin films.<sup>2</sup> (c) An expanded view of low-temperature  $\rho(T, H, n^{th})$  curves of Fig. 1. Note that (i) all  $\rho(T, n^{th})$  curves exhibit a (trace of) superconductivity; (ii) SUC transitions width ( $\Delta T_C^{10-90\%} < 80$  mK) are sharp; and that (iii) SUC is quenched on an application of  $H > H_{c2}(T, n^{th}) \approx 5$  kOe. The lines are guides to the eye.

### C. Enhancement of superconductivity

By far, the most extensively studied effect in irradiated and granular thin films is the enhancement of their superconductivity. Fig. 4 summarizes the O-incorporation-induced enhancement of  $T_c$  as obtained from this work [see Figs. 1,3(c)] as well as those reported on granular<sup>3,4</sup> and irradiated films.<sup>5-7</sup> Evidently,  $T_c$  is enhanced monotonically at lower O-incorporation, passes through a maximum and afterwards decreases monotonically.

The evolution of our  $T_c^{zero}(x)$  is in excellent agreement with the reported  $T_c^{>T_{NCR}}$  of films deposited/irradiated above  $T_{NCR}$ .<sup>9,13</sup> On the other hand, for films deposited/irradiated below  $T_{NCR}$ , their  $T_c^{<T_{NCR}}$  are higher than  $T_c^{>T_{NCR}}$ .<sup>2,6</sup> Nevertheless, each of  $T_c^{>T_{NCR}}(x)$  and  $T_c^{<T_{NCR}}(x)$  follows a dome-like evolution when plotted on a log-log scale; the maximum is attained at 2.3K (Ref. 13) for the former while at 3.2K (Ref. 2) for the latter.

Various theoretical models were suggested for the ex-

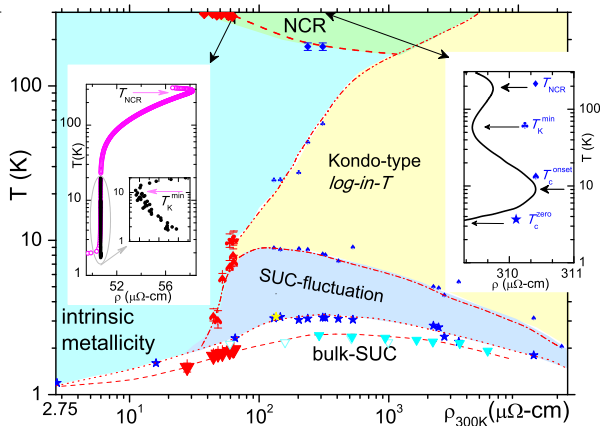


FIG. 4. Normal-state and superconducting phase diagram of various types of Aluminum thin films shown as a log-log plot of  $T$  vs  $\rho_{300K}$ . Due to aging effects, a unique room-temperature resistivity for each warming-up measuring cycle is taken to be  $\rho_{300K}^{ext}$ , represented as solid circle on the high-temperature linear extrapolation in Figs. 1, 2. The large symbols  $\blacktriangledown$ ,  $\blacklozenge$ ,  $\blacktriangle$ ,  $\blacklozenge$ :  $T_c^{zero}$ ,  $T_c^{onset}(=T_K^{max})$ ,  $T_K^{min}$ ,  $T_{NCR}$ , resp., as obtained by this work.  $\star$ ,  $\blacklozenge$ ,  $\blacktriangle$ ,  $\blacklozenge$ :  $T_c^{zero}$ ,  $T_c^{onset}(=T_K^{max})$ ,  $T_K^{min}$ ,  $T_{NCR}$  (resp., the location of each thermal event is explicitly shown at the right-side inset) of granular films deposited at 77 K (Refs. 2).  $\nabla$ ,  $\blacktriangledown$ :  $T_c$  of granular films deposited at room-temperature (Refs. 9 and 13, resp.).  $\star$ :  $T_c$  after O-implantation at liquid helium (Ref. 6). *Left-hand side inset*: A semilog plot of  $\rho(T, 6^{th}, 0$  kOe) and  $\rho(T, 6^{th}, 5$  kOe) (open and close circles, resp., see Fig. 1). *Right-hand side inset*: A semilog plot of  $\rho(T)$  curve of a granular sample having  $\rho_{300K} = 310 \mu\Omega\text{-cm}$  (see Refs. 2). The main graph is extrapolated down to  $2.75 \mu\Omega\text{-cm}$  of bulk Al.<sup>14</sup> The lines are guides to the eye.

planation of  $T_c$  enhancement [see e.g. Refs. 3, 4, 16–18]. It is recalled that  $T_c$  enhancement was observed in granular films (wherein metallic grains are nano-sized) as well as in irradiated films (wherein oxygen is implanted within the bulk and at the interface of these, similar nano-sized, grains). These observations indicate that grain-size character (spatial confinement) is not a decisive factor in  $T_c$  enhancement. As such, it is hard to relate  $T_c$  enhancement to quantum-size effects in shell structures.<sup>19</sup> Magnetic-based mechanisms can also be ruled out since  $T_c$  enhancement in Fig. 4 occurs much earlier than the region wherein possible magnetic fluctuation, if any, is expected. BCS framework, on the other hand, can not be excluded (in particular within the left-hand side of  $T_c$ -dome of Fig. 4) since it describes successfully the superconductivity of elemental Aluminum and, by extension, the lower limit of this phase diagram. Indeed,  $T_c$  enhancement had been routinely analyzed in terms of the McMillan strong-coupling formula.<sup>17</sup> Nevertheless, for a preliminary analysis, let us follow the simpler and transparent weak-limit BCS scenario. Then, a variation  $\partial T_c$  (driven by a variation in disorder/defects,  $\partial x$ ) can be expressed in terms of a sum of three contributions corresponding to a variation in Debye temperature  $\theta_D$ , in

the pairing potential  $V$  arising from electron-phonon coupling  $\lambda$ , and in the density of states  $N_F$  at Fermi energy:

$$\frac{\partial \ln T_c}{\partial x} = \frac{\partial \ln \theta_D}{\partial x} + \frac{1}{VN_F} \left( \frac{\partial \ln V}{\partial x} + \frac{\partial \ln N_F}{\partial x} \right) \quad (1)$$

Hall effect<sup>20</sup> and specific heat<sup>21</sup> measurements on granular films indicated that  $N_F$  is decreased with  $x$ . Hall effect on O-irradiated films, Fig.3(a), does confirm this trend.  $\theta_D$ , just as well, was observed to decrease with  $x$ .<sup>21</sup> Then, based on Eq.1,  $T_c$  enhancement is related to a disorder-driven increase in  $V$  which, in turn, relates to  $\lambda$ .<sup>22</sup> Indeed Fig.1(b) shows that this increase in  $\lambda$  is manifested as an increase in the metallic slope<sup>23</sup>  $(\partial \rho / \partial T)_{100-220K}$ . In fact it is almost *three-times* higher than the  $12 \text{ n}\Omega\text{-cmK}^{-1}$  reported for bulk Al.<sup>14</sup>

We associate such an increase in  $\lambda$  and  $T_c$  enhancement<sup>17,24</sup> to a softening of the lattice which is triggered by impurity-stabilized defects.<sup>25</sup> The aging of  $T_c$  is related to a partial removal of these softening-inducing defects (by recombination, sinking, etc.). Accordingly,  $T_c$  enhancement in films prepared above  $T_{NCR}$  should be smaller than  $T_c$  of films prepared below  $T_{NCR}$ : due to the action of relaxation processes (class two), the amount of softening is much less in films irradiated/deposited above  $T_{NCR}$ . Indeed, Fig. 4 confirms that  $T_c^{>T_{NCR}}(x) < T_c^{<T_{NCR}}(x)$ . Similar arguments, based on the kinetics of defects, can be advanced to explain the observed modification in each of  $T_K^{min}(x)$  and  $T_{NCR}(x)$ .

It is notable that the surge of Kondo behavior occurs just below the dome maximum of Fig. 4 [Refs.2] and that the monotonic evolution of Kondo effect is accompanied by a slowing down, a leveling out, and an eventual decay of  $T_c(x)$ . Accordingly, the dome like evolution of  $T_c(x)$  is attributed to a compromise between an enhancement trend (due to lattice softening) and a suppression trend (due to Abrikosov-Gorkov pair-breaking process). As  $T \rightarrow T_c^+$  ( $T < T_K^{min}$ ), a competition between spin-flip scattering and Cooper pairing leads to a downward deviation away from the *log-in-T* behavior and as such to an eventual resistivity maximum at  $T_K^{max}$  (see right-hand side inset of Fig. 4). When the Kondo effect is weak, it is difficult to distinguish between  $T_K^{max}$  and  $T_c$  or  $T_c^{onset}$ . In this work we followed the evolution of  $T_c^{onset}(\rho_{300K}, n^{th})$  within the region starting just before the strong surge of Kondo behavior. Fig. 4 indicates that the extrapolation of this  $T_c^{onset}(\rho_{300K})$  agrees satisfactorily with the evolution of  $T_K^{max}(\rho_{300K})$  reported for granular films.<sup>2</sup> We identify this range,  $T_c^{zero} \leq T \leq T_K^{max}$ , of Fig. 4 as being a superconducting fluctuation region.

Finally, it is interesting to check whether  $T_c$  enhancement and Kondo effect are manifested as well in other ion-irradiated superconducting thin film. First, in contrast to Al films, O-irradiation in  $\text{YBa}_2\text{Cu}_3\text{O}_x$  thin films causes a monotonic reduction in  $T_c$ , an increase in  $\rho_{300K}$ , and a transformation from a metallic into an insulating phase.<sup>26</sup> Similarly, an  $\alpha$ -irradiation of  $\text{NdFeAsO}_{1-x}\text{F}_x$  thin film induces a monotonic reduction of  $T_c$ .<sup>27</sup> A sim-

ilar irradiation-induced degradation of superconductivity was also reported in conventional Al5 and B1 thin films.<sup>28</sup> For all these films, in contrast to the strongly metallic ones, the induced weakening of the metallicity and screening suggests a scenario reminiscent of the case encountered in the right-hand side of Fig. 4.

In summary, it is shown that O-incorporation in Al thin films leads to an enhancement of  $T_c$ , to a negative curvature resistivity, and to a Kondo behavior. The obtained  $T - x$  phase diagram, similar to that of granular films, reveals the region and boundaries wherein each of

these three features is manifested. The driving mechanisms behind each of these processes are discussed.

## ACKNOWLEDGMENTS

We gratefully acknowledge the technical assistance of K. S. F. M. Araújo and the use of the facilities at LABNANO-CBPF. Partial financial supports from CNPq and Faperj are also gratefully acknowledged.

- 
- <sup>1</sup> G. Linker and O. Meyer, *Solid State Commun.* **20**, 695 (1976); G. Linker, in *Ion Implantation Into Metals*, edited by V. A. G. Procter (Pergamon, 1982) pp. 284 – 292.
- <sup>2</sup> N. Bachar, S. Lerer, A. Levy, S. Hacoheh-Gourgy, B. Almog, H. Saadaoui, Z. Salman, E. Morenzoni, and G. Deutscher, *Phys. Rev. B* **91**, 041123 (2015); N. Bachar, S. Lerer, S. Hacoheh-Gourgy, B. Almog, and G. Deutscher, *ibid.* **87**, 214512 (2013); U. S. Pracht, N. Bachar, L. Benfatto, G. Deutscher, E. Farber, M. Dressel, and M. Scheffler, *ibid.* **93**, 100503 (2016); N. Bachar, *Spin-flip Scattering in Superconducting Granular Aluminum Films*, Ph.D. thesis, Tel-Aviv University (2014).
- <sup>3</sup> B. Abeles, P. Sheng, M. Coutts, and Y. Arie, *Adv. Phys.* **24**, 407 (1975).
- <sup>4</sup> G. Deutscher, in *Superconductivity*, edited by K. Bennemann and J. Ketterson (Springer Berlin Heidelberg, 2008) p. 259.
- <sup>5</sup> A. Lamoise, J. Chaumont, F. Meunier, and H. Bernas, *J. Phys., Lett.* **36**, 271 (1975); A. Lamoise, J. Chaumont, F. Lalu, F. Meunier, and H. Bernas, *ibid.* **37**, 287 (1976).
- <sup>6</sup> A. Lamoise, J. Chaumont, F. Meunier, and H. Bernas, *J. Phys., Lett.* **36**, 305 (1975).
- <sup>7</sup> F. Meunier, P. Pfeuty, A. Lamoise, J. Chaumont, H. Bernas, and C. Cohen, *J. Phys., Lett.* **38**, 435 (1977).
- <sup>8</sup> W. Buckel, , and R. Hilsch, *Z. Physik* **138**, 109 (1954).
- <sup>9</sup> B. Abeles, R. W. Cohen, and W. R. Stowell, *Phys. Rev. Lett.* **18**, 902 (1967).
- <sup>10</sup> K. Isebeck, R. Muller, W. Schilling, and H. Wenzl, *Phys. Stat. Sol.* **18**, 427 (1966); A. Sosin and L. H. Rachal, *Phys. Rev.* **130**, 2238 (1963); W. DeSorbo and D. Turnbull, *Phys. Rev.* **115**, 560 (1959); A. Khellaf, A. Seeger, and R. M. Emrick, *Mater. Trans.* **43**, 186 (2002).
- <sup>11</sup> A. Atkinson, *Rev. Mod. Phys.* **57**, 437 (1985).
- <sup>12</sup> Y. Lassailly, A. K. Bhattacharjee, and B. Coqblin, *Phys. Rev. B* **31**, 7424 (1985); B. Coqblin and J. R. Schrieffer, *Phys. Rev.* **185**, 847 (1969); C. Lacroix, *J. Magn. Magn. Mater.* **63 & 64**, 239 (1987).
- <sup>13</sup> T. Chui, P. Lindenfeld, W. L. McLean, and K. Mui, *Phys. Rev. Lett.* **47**, 1617 (1981); *Phys. Rev. B* **24**, 6728 (1981); K. C. Mui, P. Lindenfeld, and W. L. McLean, **30**, 2951 (1984).
- <sup>14</sup> P. D. Desai, H. M. James, and C. Y. Ho, *J. Phys. Chem. Ref. Data Rep.* **13**, 1131 (1984).
- <sup>15</sup> F. T. Gamble, R. H. Bartram, C. G. Young, O. R. Gilliam, and P. W. Levy, *Phys. Rev.* **134**, A589 (1964); K. Lee, G. Holmberg, and J. Crawford, *Solid State Commun.* **20**, 183 (1976).
- <sup>16</sup> I. S. Beloborodov, A. V. Lopatin, V. M. Vinokur, and K. B. Efetov, *Rev. Mod. Phys.* **79**, 469 (2007).
- <sup>17</sup> J. W. Garland, K. H. Bennemann, and F. M. Mueller, *Phys. Rev. Lett.* **21**, 1315 (1968); J. Klein and A. Leger, *Phys. Lett. A* **28**, 134 (1968); A. Leger and J. Klein, *Phys. Lett. A* **28**, 751 (1969).
- <sup>18</sup> D. Allender, J. Bray, and J. Bardeen, *Phys. Rev. B* **7**, 1020 (1973).
- <sup>19</sup> V. Z. Kresin and Y. N. Ovchinnikov, *Physics-Uspekhi* **51**, 427 (2008); S. Bose, A. M. Garca-Garca, M. M. Ugeda, J. D. Urbina, C. H. Michaelis, I. Brihuega, and K. Kern, *Nat. Mater.* **9**, 550 (2010); J. Mayoh and A. M. García-García, *Phys. Rev. B* **90**, 134513 (2014).
- <sup>20</sup> B. Bandyopadhyay, P. Lindenfeld, W. L. McLean, and H. K. Sin, *Phys. Rev. B* **26**, 3476 (1982).
- <sup>21</sup> R. L. Greene, C. N. King, R. B. Zubeck, and J. J. Hauser, *Phys. Rev. B* **6**, 3297 (1972).
- <sup>22</sup> W. L. McMillan, *Phys. Rev.* **167**, 331 (1968).
- <sup>23</sup> P. B. Allen, T. P. Beaulac, F. S. Khan, W. H. Butler, F. J. Pinski, and J. C. Swihart, *Phys. Rev. B* **34**, 4331 (1986).
- <sup>24</sup> B. T. Matthias, G. R. Stewart, A. L. Giorgi, J. L. Smith, Z. Fisk, and H. Barz, *Science* **208**, 401 (1980).
- <sup>25</sup> Y. Kraftmakher, *Phys. Rep.* **299**, 79 (1998).
- <sup>26</sup> B. Roas, B. Hensel, G. Endres, L. Schultz, S. Klaumzner, and G. Saemann-Ischenko, *Physica C* **162**, 135 (1989); G. J. Clark, A. D. Marwick, R. H. Koch, and R. B. Laibowitz, *Appl. Phys. Lett.* **51**, 139 (1987); G. J. Clark, F. K. Legoues, A. D. Marwick, R. B. Laibowitz, and R. H. Koch, in *High-Temperature Superconductors*, edited by M. B. Brodsky, R. C. Dynes, K. Kitazawa, and H. L. Tuller (1988) pp. 127–132; H. Hilgenkamp and J. Mannhart, *Rev. Mod. Phys.* **74**, 485 (2002).
- <sup>27</sup> C. Tarantini, M. Putti, A. Gurevich, Y. Shen, R. K. Singh, J. M. Rowell, N. Newman, D. C. Larbalestier, P. Cheng, Y. Jia, and H.-H. Wen, *Phys. Rev. Lett.* **104**, 087002 (2010).
- <sup>28</sup> O. Meyer, D. Huttner, J. Geerk, T. Kroener, G. Linker, J. Rimmel, and R. Schneider, *Mat Chem. Phys.* **42**, 153 (1995).
- <sup>29</sup> J. F. Ziegler, M. Ziegler, and J. Biersack, *Nucl. Instr. Meth. B* **268**, 1818 (2010).
- <sup>30</sup> H. J. Bhatt, *Appl. Phys. Lett.* **19**, 30 (1971).
- <sup>31</sup> A. Gangulee, F. M. d’Heurle, V. A. Ranieri, and R. A. Fiorio, *J. Vac. Sci. Technol.* **16**, 156 (1979).
- <sup>32</sup> J. E. Boggio and R. C. Plumb, *J. Chem. Phys.* **44**, 1081 (1966).
- <sup>33</sup> N. Cabrera and N. F. Mott, *Rep. Prog. Phys.* **12**, 163

(1949).

- <sup>34</sup> B. P. Uberuaga, L. J. Vernon, E. Martinez, and A. F. Voter, *Sci. Rep.* **5**, 9095 (2015).  
<sup>35</sup> S. Chereckdjian and I. Wilson, *Nucl. Instrum. Methods Phys. Res., Sect. B* **1**, 258 (1984).  
<sup>36</sup> J. Geerk and O. Meyer, *Surface Science* **32**, 222 (1972).  
<sup>37</sup> R. Kelly, *Radiation Effects* **64**, 205 (1982).  
<sup>38</sup> A. Dorey and J. Knight, *Thin Solid Films* **4**, 445 (1969).  
<sup>39</sup> G. Zhigal'skii and B. Jones, *The Physical Properties of Thin Metal Films* (Taylor & Francis, 2003).

### Appendix A: Thin film synthesis, O-irradiation and characterization

Thin film of  $400\ \mu\text{m} \times 10\ \mu\text{m} \times 90\ \text{nm}$  were prepared at room temperature by sputtering of Aluminium on a lithographed Si/SiO<sub>2</sub> substrate with Ti/Au contact pads. Electron Microscopy images indicate a grain size of  $\sim 60\ \text{nm}$  which is comparable to bulk aluminum mean free path,  $l_{300\text{K}} \sim 58\ \text{nm}$ , but is much smaller than the coherence length,  $1.6\ \mu\text{m}$ .

Such thin films were irradiated with O<sup>-</sup> ions at room-temperature; seven consecutive implantation sessions were carried out (see Table I) and the influence of each irradiation was followed by resistivity measurements. During the first three sessions, the beam energies were set to 23 keV, 30 keV, and 10 keV so as to probe any dependence on implantation profile: according to simulations using the SRIM code,<sup>29</sup> these energies lead to implanted depth profiles with maxima at, respectively, sample centre, closer to Al/Si interface, and sample surface (see Table I). As that no significant dependence on the implantation profile was observed, all subsequent implantations (4<sup>th</sup> to 7<sup>th</sup>) were performed with a beam of 23 keV.

There is a vast literature on the structural, magnetic and resistive properties of the O-incorporated granular Al thin films<sup>2-4,30</sup> as well as on O-irradiated Al thin film.<sup>5-7,31</sup> As our irradiated films were prepared by the same recipe, they proved to be intrinsically similar to the ones reported in previous works. Considering that our main interest is to map out their normal and superconducting phase diagram, we carried out extensive DC/AC four-points resistivities both *in situ* during irradiations as well as *ex situ*. The *ex situ* ones were measured as a function of time, temperature, magnetic field and fluence after each  $n^{\text{th}}$  irradiation session:  $\rho(t, T, H, n^{\text{th}})$ . The obtained results compare favorably with the ones reported for granular<sup>2-4</sup> and irradiated films.<sup>5-7</sup> Hall measurements on representative samples confirmed the earlier findings<sup>20</sup> that the major charge carriers are electrons and their density is decreased with irradiation.

Based on analysis of thermal evolution of  $\rho(t, T, H, x)$ , we identified all transition/crossover events in each curve; specifically,  $T_K^{\text{max}}(x)$  and  $T_{\text{NCR}}(x)$  are signalled by maximums,  $T_K^{\text{min}}(x)$  by a minimum,  $T_c^{\text{onset}}(x)$  by an onset point or a downward deviation away from normal-state resistivity, and  $T_c^{\text{zero}}(x)$  by a transition point whereat  $\rho(T, x) \rightarrow 0$ . On the other hand, for a quantification and

a measure of the content of disorder/defects, denoted as  $x$ , we followed the usual and convenient practice of taking  $x$  to be the room-temperature resistivity, i.e.  $x \equiv \rho_{300\text{K}}(t, n^{\text{th}})$ ; this is adopted for both the granular<sup>2-4</sup> and irradiated thin films.<sup>5-7</sup> For our *O-irradiated* Al thin films, due to the presence of relaxation processes, it is better to use the extrapolated  $\rho_{300\text{K}}^{\text{ext}}(t, n^{\text{th}})$  [see Figs.2(a) and 4]. It is possible to utilize, instead,  $\rho_{T \rightarrow 0\text{K}}(t, n^{\text{th}})$ , but this would not modify any of the conclusions reached in this work. A plot of the above-determined temperature points gives the  $T - x$  phase diagram of the O-irradiated thin films.

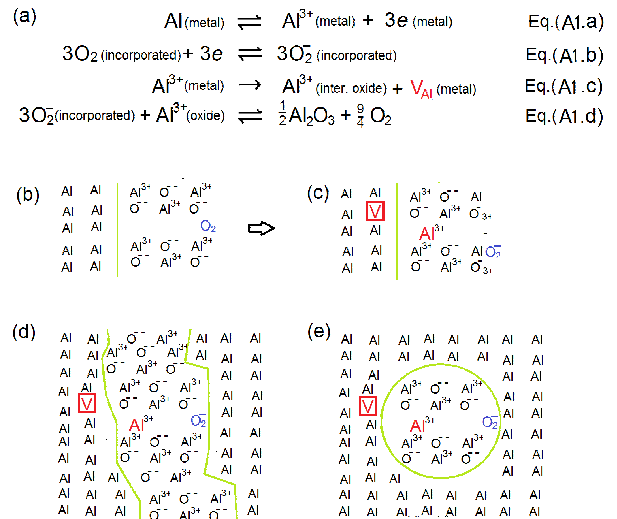


FIG. 5. (a) A multi-step kinetic scheme for oxidation of Aluminum as described in the Cabrera-Mott model (adapted from Ref.32). Directly after ionization (Eq. A1.a),  $3e$  pass freely through the oxide interface till reaching incorporated oxygen which are then ionized to  $\text{O}_2^-$  (Eq. A1.b). This charge transfer together with the left-behind positive  $\text{Al}^{3+}$  induce a local electric field which drives the slow migration of  $\text{Al}^{3+}$  across the oxide interface leaving behind a vacancy  $\text{V}_{\text{Al}}$  (Eq. A1.c). Eq. A1.d indicates a typical formation of  $\text{Al}_2\text{O}_3$  by the combination of migrated  $\text{Al}^{3+}$  and ionized  $\text{O}_2^-$ . (b-c) An illustration of the reaction at metal-oxide interface (represented by the solid green line) of a directly exposed film [(b) is before the reaction while (c) is after the third step; adapted from Ref.11]. (d) An interaction similar to that described in (a) and (b) but at the boundary interface of a granular film. (e) Similar reaction occurring at the boundary of an isolated oxide grain of an irradiated film. In all cases, incorporated and ionized oxygen are represented, with no loss of generality, by  $\text{O}_2$  and  $\text{O}_2^-$ . It is worth mentioning that oxidation in both the granular and irradiated films, in contrast to the exposed case, occurs within the film bulk and, furthermore, the involved quantity of oxygen is fixed after ending the incorporation process.

We depicted, on the very same plot of Fig. 4, various previously reported  $T - \rho_{300\text{K}}(x)$  data of granular<sup>2-4</sup> and irradiated thin films.<sup>5-7</sup> It is remarkable that all data, new and old, follow the same phase boundary lines: that *all* lines join together across the whole available disorder

TABLE I. The beam energy, partial and accumulated fluence, and peak centre of the depth profile for each of the consecutive implantation sessions used in this work.

Irradiation	Energy keV	Peak of depth profile <sup>a</sup> <i>nm</i>	Fluence 10 <sup>16</sup> ions/cm <sup>2</sup>	Accumulated Fluence 10 <sup>16</sup> ions/cm <sup>2</sup>
1	23	50	0.42	0.42
2	10	23	0.34	0.76
3	30	64	0.5	1.26
4	23	50	1.21	2.47
5	23	50	1.25	3.72
6	23	50	1.77	5.49
7	23	50	0.97	6.46

<sup>a</sup>Estimated using the SRIM code.<sup>29</sup>

region is a finding which is far from being trivial.

### Appendix B: The two classes of relaxation processes

The simplest method of O-incorporation into Aluminum thin film is a direct exposure to an oxygen gas.<sup>11</sup> The kinetics of oxidation of such a film is usually considered within the Cabrera and Mott model:<sup>33</sup> a multi-step process that involves charges transfer as well as ionic/vacancies migrations (see schematic illustration in Fig. 5). This very same Cabrera-Mott process (from individual Al and O atoms up to a formation of Al<sub>2</sub>O<sub>3</sub>) is envisaged as occurring in both the granular and irradiated films. However, in contrast to oxidation in directly-exposed or granular films, low-energy O-irradiation involves a creation of a large number of unstable defects (e.g. vacancies, interstitial Al or oxygen, etc.) that interact with each other and with impurities.<sup>34</sup>

Diffusive motion of these defects facilitates their recombination/sinking and also assist in the formation of dislocation loops and eventually Al<sub>2</sub>O<sub>3</sub> precipitates.<sup>35-37</sup> Obviously, the very action of O-irradiation forces the film away from thermodynamic equilibrium; as a consequence, during and after each irradiation session, thermally-assisted relaxation processes are required to reestablish equilibrium. We distinguish two classes of such relaxation processes.

The first class consists of conventional relaxation processes that are routinely observed in pure Aluminum when irradiated by high-energy neutrons<sup>10</sup> or electrons<sup>10</sup> or simply after being fast-quenched from a high-temperature.<sup>10</sup> In all cases, the total resistivity recovers back to its equilibrium value through the action of relaxation processes which, for pure Aluminum, are manifested as three recovery stages:<sup>10</sup> stage I is dominant below  $\sim 50$  K; stage II is centered at  $\sim 140$  K, while stage III operates within  $190 < T < 250$  K range.

The second class consists of relaxation processes which are much slower (in days) than those of the first class and appear when there are sufficient implanted chemically-active oxygen either as projectiles leading to a forma-

tion of impurity centres that stabilizes other irradiation-induced defects (thus affecting recovery by trapping vacancies/interstitial or by being adsorbed on dislocations and thereby inhibiting their climb<sup>10</sup>) or as oxidizing agents that eventually lead to a formation of Al<sub>2</sub>O<sub>3</sub>.<sup>11</sup> Below we emphasize the role of the second class in shaping the normal and superconducting phase diagrams of these O-incorporated thin films.

### Appendix C: Thermal and temporal evolution of electric resistivity in O-irradiated thin films

Resistivity is one of the simplest technique to probe the above mentioned two classes. As an illustration, a recovery curve of resistivity of pure Aluminum films after being fast-quenched from high-temperature exhibits two types of first-class processes:<sup>10</sup> a first-order process related to a migration of single vacancy or self- interstitial to sinks and a second-order one related to a mutual annihilation of interstitial with vacancies. If the decay rate is taken as  $\partial\rho_d/\partial t = k_1\rho_d + k_2\rho_d^2$ , then the isothermal defect resistivity follows<sup>10</sup>

$$\rho_d(t, T) = \frac{k_1}{\left[ \frac{k_1}{\rho_d(0, T)} + k_2 \right] e^{k_1 t} - k_2} \quad (C1)$$

wherein  $k_i \propto e^{-\frac{E_i}{T}}$  and  $E_i$  is an  $i^{th}$  activation energy. An alternative, simpler but less transparent, analytical expression for  $\rho_d$  assumes a single, rate-determining, thermally-activated process with a decay rate being  $\partial\rho_d/\partial t = -Ae^{-\frac{\Delta}{T}} e^{B\rho_d}$  ( $A, B$  are constant;  $\Delta$  is an effective activation energy; on low order expansion this rate approximates that of Eq.C1). Then,  $\rho_d(t, T)$  evolves as (see Fig. 6):<sup>38</sup>

$$\rho_d(t, T) = -B^{-1} \ln(ABte^{-\frac{E}{T}} + e^{-B\rho_d(0, T)}) \quad (C2)$$

For our irradiated films, an insight into the individual role of each of the above-mentioned two relaxation classes can be gained when monitoring the time evolution of isothermal resistivity,  $\rho(t, 300\text{K}, n^{th})$ , during and

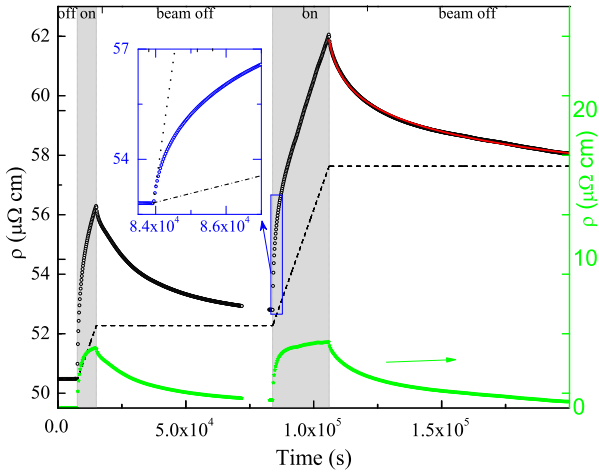


FIG. 6.  $\rho(t, 300\text{K}, 6^{\text{th}})$  measured with a current density  $j=10^7 \text{ A/m}^2$  during two consecutive O-irradiation sessions without breaking a vacuum of  $1.0 \times 10^{-7}$  Torr. The irradiation intervals are shown as vertical grey areas. *Inset* highlights the presence of relaxation processes: in their absence, the resistivity rise should have followed the dotted line (expected in films prepared below  $T_{DLR}$ ). During the steady state, the resistivity rises linearly with a rate given by dot-dash line in inset. The dashed lines simulate a situation wherein the irradiation process is considered as if proceeding with the rate of the steady state and that directly after the beam stoppage, one assumes idealized two contributions: a fast-decaying contribution (depicted as green stars with a height indicated by the right-hand y-axis) and a slow contribution (depicted as a horizontal dashed lines).  $\rho_d(t > 106000\text{s}, 300\text{K}, 6^{\text{th}})$  is a tentative fit to the empirical Eq.C2 (solid red line) with  $A=0.0018(1) \mu\Omega\text{-cm/s}$ ,  $B=0.91(1) [\mu\Omega\text{-cm}]^{-1}$ ,  $E=1574(89) \text{ K}$ ,  $\rho_d^0=4.451(1) \mu\Omega\text{-cm}$ .

directly after the O-irradiation. Fig.6 exhibits a typical  $\rho(t, 300\text{K}, 6^{\text{th}})$  curve of two consecutive beam-On-beam-Off irradiation sessions without breaking the vacuum. Evidently, at the start of each irradiation, the quasi exponential rise of resistivity indicates that the generation of defects is faster than their removal. When a steady state is reached, the resistivity rises linearly with time suggesting that  $\Delta\rho_d \propto \Delta N_d$  (the constantly injected, excess defect concentration).<sup>39</sup> When irradiation beam is turned off, the total resistivity was analyzed as a sum of the following two contributions:

The first is a relatively fast-decaying contribution; it is related to the above-mentioned first class of relaxation processes (describable by, say, any of Eqs. C1-C2). However, different from the case of pure Aluminum the total resistivity does not recover its equilibrium value before the last irradiation. Below we argue that the time evolution (in days) of  $T_c(t, x)$ ,  $T_K^{\text{min}}(t, x)$  and  $T_{\text{NCR}}(t, x)$  as well as that of *ex situ*  $\rho_{300\text{K}}(t, x)$  are governed by the second class of relaxation processes.

This second contribution is evident after subtracting the above mentioned fast-decaying first-class contribution from the total resistivity after beam stoppage: the

result is the dashed line in Fig.6; within a short time interval, the remaining contribution looks quasi static if compared with that of the first class: hence the idealization by a horizontal dashed line in Fig.6. However, further measurements revealed a slowly decaying contribution which is best seen in the measurements of repeated cooling-warming cycles of Figs.1-2: after each  $n^{\text{th}}$  irradiation, the films is cooled to helium temperatures and afterwards  $\rho(T, n^{\text{th}})$  is measured, on warming, up to above room temperature. Specifically, for the  $7^{\text{th}}$  irradiation, this process was repeated five times (see Fig.2) and their evolution reveal a strong aging influence on the characteristic temperatures: the superconducting  $T_c(t, 7^{\text{th}})$  is degraded, the Kondo  $T_K^{\text{min}}(t, 7^{\text{th}})$  is decreased while the negative curvature peak centre (maximum) at  $T_{\text{NCR}}(t, 7^{\text{th}})$  is increased. After two months, there is hardly any change in these  $T_c$ ,  $T_K^{\text{min}}$ , and  $T_{\text{NCR}}$ .

#### Appendix D: Influence of kinetics of defects on the negative curvature resistivity (NCR)

We associated the Kondo effect to a surge of irradiation-induced paramagnetic centers while the enhancement of superconductivity to an irradiation-induced softening of the lattice. Fig.2 indicates that NCR is strongly correlated with the superconductivity enhancement and Kondo effect; then it is inferred that NCR must be driven by a mechanism which is related to impurity-stabilized defects; we suggest two related scenarios: (i) An annihilation of impurity-stabilized defects: a thermally activated irreversible process, much accelerated above  $T_{\text{NCR}}$ , which leads to a drop in the total resistivity; such a drop is manifested in the lowering of  $\rho_{300\text{K}}(t, n^{\text{th}})$  and  $\rho_{0\text{K}}(t, n^{\text{th}})$ . (ii) A thermal disassociation of trapped electric charge occurring when the temperature is increased above  $T_{\text{NCR}}$ ; such charges include electrons (trapped at an anion vacancy) or holes/hole-pairs (trapped near an oxygen ion which is adjacent to  $\text{Al}^{3+}$  vacancy); if a steady state is reached, then this disassociation/association process is reversible-*in-T* leading to a reproducible NCR peak at  $T_{\text{NCR}}$  (observed after a long time). It is worth mentioning that studies on  $\gamma$ -irradiated  $\text{Al}_2\text{O}_3$  identified a thermally-activated dissociation of hole pairs into single hole at 384 K and an annihilation of holes at 533 K.<sup>15</sup> That the temperature range in our case is lower than that manifested in  $\gamma$ -irradiated  $\text{Al}_2\text{O}_3$  is most probably related to the difference in the kinetics of defects: it is then no surprise that aging triggers an increase in  $T_{\text{NCR}}$  (towards the disassociation point observed in  $\text{Al}_2\text{O}_3$ ).<sup>15</sup>

It is worth recalling that in O-incorporated Al films, the impurities are mainly due to  $\text{Al}_2\text{O}_3$  chemical complex rather than to individual oxygen (similar to the case of irradiated Molybdenum thin films<sup>1</sup>). As such, most of these impurity-stabilized defects are expected to be located at the border between metallic grains and  $\text{Al}_2\text{O}_3$  interface. A fraction of these defects acts as nu-

cleating centres for the paramagnetic moments while another fraction participates in trapping the holes/hole-pairs. A reduction of these defects leads to (i) a reduction of scattering centres (aging of  $\rho_{300\text{K}}$ ), (ii) a reduction of the thermally-activated disassociation/annihilation of

trapped holes above  $T_{\text{NCR}}$  (the point above which such processes are dominant), (iii) a reduction of the paramagnetic centres (lowering of  $T_{\text{K}}$ ) and (iv) a reduction in lattice softening (degradation of  $T_{\text{c}}$ ) (see Fig.2).